

INFORMATIVE PATH PLANNING BASED ON REDUCED-RANK GAUSSIAN PROCESS FOR HAZARDOUS SUBSTANCE MONITORING

Changmin Lee[1] & Minkyu Park[1*]

[1]Department of Artificial Intelligence Convergence Engineering, Changwon National University, Changwon, Republic of Korea

Abstract

This study proposes an integrated framework for real-time informative path planning and hazardous-substance mapping using an unmanned aerial vehicle (UAV) in an environment where hazardous materials are released from multiple container structures. To account for the characteristics of mobile sensor measurements collected during UAV operation, an Extended Reduced-Rank Gaussian Process (ERRGP) is proposed to handle non-Gaussian measurement models and is formulated to be applicable to various types of sensors. For path planning, the proposed framework utilizes LiDAR-based frontiers to generate active exploration trajectories that maximize information gain while avoiding obstacles. The proposed framework is validated through simulation experiments.

Keywords: Informative path planning, Environmental mapping, Reduced-rank Gaussian Process, Robot information gathering

1. Introduction

In environments contaminated by hazardous substances such as radiation, toxic gasses, and chemical pollutants, rapid and safe situational awareness is essential. In such environments, human access is often restricted, and direct intervention may cause secondary damage. Therefore, environmental monitoring technologies based on remote or autonomous systems are required [1]. In particular, the spatial distribution of hazardous substances is generally nonuniform because it is affected by the locations of sources, shielding structures, obstacle arrangements, and attenuation effects. Consequently, it is difficult to accurately assess the entire field by measuring sensor values only at specific locations. Therefore, informative path planning is important for quantitatively estimating the spatial distribution of hazardous substances from limited sensor measurements while actively determining the next measurement locations [2].

Unlike ground robots, an unmanned aerial vehicle (UAV) is not restricted to traversable ground regions and can move freely in three-dimensional (3D) space while collecting sensor measurements at different altitudes. This capability is particularly important in industrial environments or accident sites that include vertical structures such as chimneys, containers, and shielding objects. By using a UAV, upper regions and 3D spaces around obstacles that are difficult for ground robots to access can be observed [3]. In addition, sensor measurements may vary with the UAV flight altitude and the 3D distance between the UAV and the radiation sources. Therefore, hazardous-substance monitoring using an aerial platform requires 3D environmental mapping that accounts for both position and altitude, rather than a two-dimensional planar map. Accordingly, this study addresses the problem of real-time radiation field estimation using UAV-based sensor measurements in a 3D hazardous environment containing multiple radiation sources inside container structures.

Various regression methods, including interpolation [4], support vector regression [5], kriging [6], and Gaussian Process Regression (GPR) [7, 8], have been used for environmental field mapping.

https://doi.org/10.71945/icas2026_0513

However, many existing approaches consider only the predicted field values and cannot quantitatively represent predictive uncertainty. Since information theory quantifies uncertainty about the target field, both prediction and uncertainty must be considered to design an informative path planning strategy. Although kriging [6] and GPR [7, 8] can provide uncertainty estimates, kriging has limitations in accounting for measurement noise and real-time scalability. In contrast, GPR models the underlying function as a stochastic process, enabling spatial correlations and uncertainty to be represented in an integrated manner. In addition, kernel functions allow the physical characteristics of the environment to be directly incorporated into the model.

However, standard GPR has a computational complexity of $O(n^3)$ with respect to the number of measurements n, which causes the computational cost to increase rapidly when sensor data are collected and accumulated in real time during UAV flight. Previous studies on radiation field prediction have mainly adopted offline approaches in which a sensor platform follows a predetermined path, collects data, and constructs a radiation distribution map using GPR after data collection is completed [9, 8]. To address the computational complexity of GPR, approximation methods such as Sparse GPR (SGPR) [10], the Generalized Robust Bayesian Committee Machine (GRBCM) [11], and the Reduced-Rank Gaussian Process (RRGP) [12] have been investigated. SGPR and GRBCM require retraining using the entire dataset whenever new data are collected, whereas RRGP reduces the computational cost by approximating the process as a linear combination of basis functions. Moreover, by sequentially updating the mean and covariance using a Kalman filter, RRGP can update both predicted values and uncertainties in real time as new measurements arrive [13]. This makes RRGP suitable for real-time path planning even on low-power onboard computing platforms.

Meanwhile, the outputs of hazardous-substance sensors such as radiation sensors are not continuous measurements with Gaussian noise, but count-based data representing the number of particles detected over a fixed time interval. Such data generally follow a Poisson distribution [8]. Therefore, this study extends the conventional RRGP and proposes an Extended Reduced-Rank Gaussian Process (ERRGP) model that accounts for the non-Gaussian characteristics of radiation sensor measurements. The proposed model can sequentially update the radiation field estimate using sensor data that follow a non-Gaussian distribution, thereby enabling real-time estimation of both the contaminant distribution and its uncertainty.

This study proposes a UAV-based framework for 3D hazardous-substance mapping and informative path planning. The proposed framework observes surrounding obstacles using 3D LiDAR and updates a 3D occupancy map based on the acquired measurements. Subsequently, radiation count measurements collected at the current 3D UAV position are sequentially incorporated into the ERRGP model to update the predictive mean and variance of the hazardous-substance field. In the path planning stage, 3D candidate points are generated within the currently observed free space, and the information gain of each candidate point is computed by combining the ERRGP predictive variance with frontier information [14]. The ERRGP variance is used as an exploitation metric for selecting regions with high uncertainty in the hazardous-substance field, while the frontier information is used as an exploration metric for encouraging expansion into insufficiently explored regions.

To validate the performance of the proposed method, predictions were generated from noisy sensor data collected by a UAV during exploration in a simulation environment and quantitatively compared with the ground-truth radiation field. The main contributions of this study are summarized as follows:

1. An Extended Reduced-Rank Gaussian Process (ERRGP) model is proposed by extending the conventional Reduced-Rank Gaussian Process to account for radiation sensor data with non-Gaussian characteristics collected in 3D space. The proposed model can estimate the predictive mean and variance in real time by considering the probabilistic characteristics of the collected sensor data.

2. An informative path planning framework is designed by integrating an ERRGP-based information gain function with obstacle information, enabling efficient exploration target selection and safe path generation in 3D environments suitable for UAV operation.

3. The proposed UAV-based informative path planning framework is validated in a 3D simulation environment containing multiple radiation sources and shielding structures, demonstrating the

feasibility of 3D hazardous-substance field mapping using limited sensor measurements.

The remainder of this paper is organized as follows. section 2. describes the ERRGP-based radiation field modeling method. section 3. presents the informative path planning framework. section 4. provides the simulation results, and section 5. concludes the paper and discusses future work.

2. Regression Model

This section describes the probabilistic regression model used for UAV-based 3D radiation field mapping. Since the UAV collects radiation sensor measurements in 3D space, each measurement location is defined as $\mathbf{x} = [x^{(1)}, x^{(2)}, x^{(3)}]^\top \in \mathbb{R}^3$, where $x^{(1)}$, $x^{(2)}$, and $x^{(3)}$ denote the spatial coordinates of the UAV within the 3D domain. A Gaussian Process (GP) is a non-parametric regression model that defines a distribution over functions as a stochastic process for supervised learning problems [15]. A GP is specified by a mean function and a kernel function, enabling the prediction of values at unmeasured locations by exploiting the spatial correlation between input locations. In particular, because a GP provides both the predictive mean and predictive variance, it has been widely used in various regression and interpolation problems.

In this study, we first introduce the Poisson likelihood Gaussian Process (PGP) to account for the fact that radiation sensor outputs are count-based measurements that follow a Poisson distribution [8]. We then summarize the basic structure of the Reduced-Rank Gaussian Process (RRGP) designed for real-time computation [13]. Finally, we present the Extended Reduced-Rank Gaussian Process (ERRGP), which integrates the Poisson likelihood with the RRGP structure.

2.1 Poisson Gaussian Process

Radiation fields exhibit nonlinear spatial distributions because gamma rays emitted from radiation sources interact with air and surrounding structures, resulting in attenuation and shielding effects. When a UAV collects radiation sensor measurements at different positions and altitudes, the sensor values vary depending on the 3D distance between the radiation source and the UAV, the spatial arrangement of shielding structures, and air attenuation effects [8, 16].

The output of a radiation sensor is count-based data expressed in counts per second (CPS), representing the number of particles detected over a fixed time interval. These data take non-negative integer values and exhibit the characteristics of a Poisson distribution, in which the mean and variance are inherently coupled. Accordingly, let the i-th measurement location of the UAV be denoted as $\mathbf{x}_i = [x_i^{(1)}, x_i^{(2)}, x_i^{(3)}]^\top \in \mathbb{R}^3$, and let the corresponding sensor measurement be denoted as $y_i \in \mathbb{Z}_{\geq 0}$. Then, the measurement can be modeled using the following Poisson likelihood:

$$y_i \sim \text{Poisson}(\lambda_i), \qquad \lambda_i = \exp(f(\mathbf{x}_i)) \tag{1}$$

Here, λ_i denotes the Poisson rate parameter obtained by mapping the latent function $f(\mathbf{x}_i)$ through an exponential link function. The latent function $f(\mathbf{x})$ is modeled as a GP:

$$f(\mathbf{x}) \sim \mathcal{GP}\big(m(\mathbf{x}), k(\mathbf{x}, \mathbf{x}')\big) \tag{2}$$

Here, $m(\mathbf{x})$ denotes the mean function, and $k(\mathbf{x}, \mathbf{x}')$ denotes the kernel function. The kernel function defines the correlation between two locations $\mathbf{x}$ and $\mathbf{x}'$ in 3D space, representing the spatial continuity and local variations of the radiation field. In this study, a composite kernel consisting of a Matérn 3/2 kernel and a Bias kernel is employed to capture local variations, smooth attenuation characteristics, and background radiation components of the radiation field:

$$k(\mathbf{x}, \mathbf{x}') = \sigma_f^2 \left(1 + \frac{\sqrt{3}\|\mathbf{x} - \mathbf{x}'\|}{l}\right) \exp\left(-\frac{\sqrt{3}\|\mathbf{x} - \mathbf{x}'\|}{l}\right) + \sigma_b^2 \tag{3}$$

Here, σ_f^2 denotes the signal variance of the Matérn kernel, l denotes the length scale, and σ_b^2 denotes the variance of the Bias kernel. The term $\|\mathbf{x} - \mathbf{x}'\|$ represents the 3D Euclidean distance:

$$\|\mathbf{x} - \mathbf{x}'\| = \sqrt{(x^{(1)} - x'^{(1)})^2 + (x^{(2)} - x'^{(2)})^2 + (x^{(3)} - x'^{(3)})^2} \tag{4}$$

The PGP framework defined above is a nonlinear Bayesian regression model that places a GP prior on the latent function and adopts a Poisson distribution as the observation likelihood. However, since the Poisson likelihood is non-Gaussian, the posterior distribution $p(f \mid \mathbf{y})$ cannot be analytically derived in a closed Gaussian form. Therefore, a Laplace approximation is employed to approximate the posterior distribution as a Gaussian distribution:

$$p(f \mid \mathbf{y}) \approx \mathcal{N}\left(f_{\text{MAP}}, \mathbf{H}^{-1}\right), \quad \mathbf{H} = \nabla_f^2 [-\log p(\mathbf{y} \mid f) - \log p(f)] \Big|_{f=f_{\text{MAP}}} \tag{5}$$

Here, f_{MAP} denotes the maximum a posteriori (MAP) estimate of the latent function, and $\mathbf{H}^{-1}$ represents the posterior covariance approximated by the inverse Hessian evaluated at f_{MAP}.
Although PGP effectively captures the non-Gaussian, count-based characteristics of radiation sensor measurements, its computational complexity scales as $O(n^3)$ with respect to the number of measurements n. As a result, computation becomes prohibitively expensive when sensor data are accumulated in real time during UAV flight. The following section introduces the Reduced-Rank Gaussian Process, which approximates the GP to mitigate this computational burden.

2.2 Reduced-Rank Gaussian Process

Although GPR has high expressive capability, its computational cost increases significantly as the number of data points grows due to the inversion of the kernel matrix. The Reduced-Rank Gaussian Process (RRGP) reduces the computational complexity of GP by approximating a stationary kernel with a finite set of basis functions [12]. In this study, the input dimension is defined as $d = 3$ to model the measurements collected by the UAV in 3D space, and the RRGP basis-function expansion is defined for the 3D measurement location $\mathbf{x} = [x^{(1)}, x^{(2)}, x^{(3)}]^\top$.
In RRGP, the kernel function $k(\mathbf{x}, \mathbf{x}')$ is approximated as a finite linear combination of m eigenfunctions as follows:

$$k(\mathbf{x}, \mathbf{x}') \approx \sum_{j=1}^{m} S(\lambda_j) \phi_j(\mathbf{x}) \phi_j(\mathbf{x}') \tag{6}$$

Here, $S(\lambda_j)$ denotes the spectral density, $\phi_j(\mathbf{x})$ denotes the j-th eigenfunction, and λ_j^2 denotes the corresponding eigenvalue. In this study, the 3D domain of interest Ω, in which the UAV collects measurements during flight, is defined as follows:

$$\Omega = [-L_1, L_1] \times [-L_2, L_2] \times [-L_3, L_3] \tag{7}$$

Here, L_1, L_2, and L_3 denote the half-widths of the centered coordinate system along the $x^{(1)}$, $x^{(2)}$, and $x^{(3)}$ directions, respectively. The actual UAV position in the world coordinate system is transformed into the centered coordinate system during computation. Under Dirichlet boundary conditions, the eigenfunction in the 3D domain is expressed as follows:

$$\phi_j(\mathbf{x}) = \sqrt{\frac{1}{L_1 L_2 L_3}} \sin\left(\frac{\pi n_{j,1}(x^{(1)} + L_1)}{2L_1}\right) \sin\left(\frac{\pi n_{j,2}(x^{(2)} + L_2)}{2L_2}\right) \sin\left(\frac{\pi n_{j,3}(x^{(3)} + L_3)}{2L_3}\right) \tag{8}$$

Here, $n_{j,1}$, $n_{j,2}$, and $n_{j,3} \in \mathbb{N}$ denote the mode indices along the $x^{(1)}$, $x^{(2)}$, and $x^{(3)}$ directions, respectively. The corresponding eigenvalue is defined as follows:

$$\lambda_j^2 = \left(\frac{\pi n_{j,1}}{2L_1}\right)^2 + \left(\frac{\pi n_{j,2}}{2L_2}\right)^2 + \left(\frac{\pi n_{j,3}}{2L_3}\right)^2 \tag{9}$$

Let the set of measurement locations be denoted as $\mathbf{X} = [\mathbf{x}_1, \mathbf{x}_2, \ldots, \mathbf{x}_n]^\top$. Then, the design matrix $\mathbf{\Phi} \in \mathbb{R}^{n \times m}$ is defined as follows:

$$\mathbf{\Phi}_i = [\phi_1(\mathbf{x}_i), \phi_2(\mathbf{x}_i), \ldots, \phi_m(\mathbf{x}_i)] \tag{10}$$

Using this design matrix, the kernel matrix $\mathbf{K} \in \mathbb{R}^{n \times n}$ is approximated in a low-dimensional form as follows:

$$\mathbf{K} \approx \mathbf{\Phi} \mathbf{\Lambda} \mathbf{\Phi}^\top \tag{11}$$

Here, $\mathbf{\Lambda} \in \mathbb{R}^{m \times m}$ is a diagonal matrix containing the prior variances of the basis-function coefficients and is defined as follows:

$$\mathbf{\Lambda} = \mathrm{diag}\,(S(\lambda_1), S(\lambda_2), \ldots, S(\lambda_m)) \tag{12}$$

Therefore, in RRGP, the latent function $f(\mathbf{x})$ is expressed as a linear combination of basis functions:

$$f(\mathbf{x}) = \boldsymbol{\phi}(\mathbf{x})^\top \mathbf{w}, \qquad \mathbf{w} \sim \mathcal{N}(\mathbf{0}, \mathbf{\Lambda}) \tag{13}$$

Here, $\boldsymbol{\phi}(\mathbf{x}) = [\phi_1(\mathbf{x}), \phi_2(\mathbf{x}), \ldots, \phi_m(\mathbf{x})]^\top$, and $\mathbf{w} \in \mathbb{R}^m$ denotes the vector of basis-function coefficients. In a standard RRGP with a Gaussian likelihood, the observation model can be expressed in the following linear form:

$$y_i = \mathbf{\Phi}_i \mathbf{w} + \varepsilon_i \tag{14}$$

Here, y_i denotes a continuous observation under the Gaussian likelihood assumption, and ε_i denotes Gaussian measurement noise. In this structure, the mean and covariance of $\mathbf{w}$ can be treated as state variables and sequentially updated using a Kalman filter [13]. Therefore, the mean and covariance can be updated in real time whenever new data are received, without repeatedly using all measurements to recompute the full kernel matrix.

However, radiation sensor data are not continuous measurements that follow a Gaussian likelihood, but count-based data that follow a Poisson distribution. Therefore, a standard RRGP cannot be directly applied to radiation sensor measurements. The following section describes the Extended Reduced-Rank Gaussian Process, which integrates the Poisson likelihood with the RRGP structure for real-time processing of 3D radiation sensor measurements collected during UAV flight.

2.3 Extended Reduced-Rank Gaussian Process

The Poisson Gaussian Process (PGP) described in subsection 2.1 can account for the non-Gaussian characteristics of radiation sensor measurements. however, as in standard GP inference, its computational cost increases rapidly as the size of the kernel matrix grows. In contrast, the Reduced-Rank Gaussian Process (RRGP) described in subsection 2.2 improves computational efficiency by approximating the kernel with a finite set of basis functions and sequentially updating the mean and covariance of the basis-function coefficients. Nevertheless, standard RRGP assumes a Gaussian likelihood and therefore cannot directly accommodate count-based radiation sensor measurements that follow a Poisson distribution.

To address these limitations, this study proposes an Extended Reduced-Rank Gaussian Process (ERRGP), which combines the Poisson likelihood with the RRGP structure. ERRGP preserves the Poisson likelihood structure of radiation sensor measurements while limiting the dimension of the state vector by representing the latent function with a finite set of basis functions. This enables sensor data collected by the UAV during flight in 3D space to be incorporated in real time, and allows the predictive mean and uncertainty of the radiation field to be sequentially updated. As in the kernel used in Eq. (3), this study uses a composite kernel consisting of a Matérn 3/2 kernel and a Bias kernel. The Bias kernel represents a spatially independent constant component and is used to represent background radiation or the overall background component. The Bias kernel can be separated and expressed as a constant basis function as follows.

$$\phi_0(\mathbf{x}) = 1, \qquad k_{\mathrm{bias}}(\mathbf{x}, \mathbf{x}') = \sigma_b^2 \phi_0(\mathbf{x}) \phi_0(\mathbf{x}') \tag{15}$$

In contrast, because the Matérn 3/2 kernel is a stationary kernel, the reduced-rank approximation described in Eq. (6) can be applied. Therefore, the Matérn 3/2 kernel component is approximated using a finite set of eigenfunctions. The spectral density of a general Matérn kernel can be expressed as a function of the input dimension d and the smoothness parameter ν as follows.

$$S(\lambda_j) = \sigma_f^2 \frac{(2\nu)^\nu \Gamma(\nu + d/2)}{\Gamma(\nu) \pi^{d/2} l^{2\nu}} \left(\frac{2\nu}{l^2} + \lambda_j^2 \right)^{-(\nu + d/2)} \tag{16}$$

In this study, the Matérn 3/2 kernel is used, and thus $\nu = 3/2$. Since the UAV measurement locations are used as 3D inputs, $d = 3$. Therefore, the spectral density in Eq. (16) is evaluated with respect

to the 3D eigenvalue λ_j^2 and used as the prior variance of each basis function. By combining the Bias kernel and the reduced-rank approximation of the Matérn 3/2 kernel, the complete kernel is approximated as follows.

$$k(\mathbf{x},\mathbf{x}') \approx \sigma_b^2 \phi_0(\mathbf{x})\phi_0(\mathbf{x}') + \sum_{j=1}^{m} S(\lambda_j)\phi_j(\mathbf{x})\phi_j(\mathbf{x}') \tag{17}$$

By adding the Bias term to the design matrix in Eq. (10), the design matrix row can be expressed as follows.

$$\mathbf{\Phi}_i = [\phi_0(\mathbf{x}_i), \phi_1(\mathbf{x}_i), \phi_2(\mathbf{x}_i), \ldots, \phi_m(\mathbf{x}_i)] \tag{18}$$

The prior covariance matrix of the basis-function coefficients is defined by including the Bias component and the spectral weights of the Matérn 3/2 components as follows.

$$\mathbf{\Lambda} = \operatorname{diag}\left(\sigma_b^2, S(\lambda_1), S(\lambda_2), \ldots, S(\lambda_m)\right) \tag{19}$$

Using this representation, the latent function $f(\mathbf{x})$ is expressed as a linear combination of basis functions as follows.

$$f(\mathbf{x}) = \boldsymbol{\phi}(\mathbf{x})^\top \mathbf{w}, \qquad \mathbf{w} \sim \mathcal{N}(\mathbf{0}, \mathbf{\Lambda}) \tag{20}$$

Here, $\mathbf{w} \in \mathbb{R}^{1+m}$ denotes the state vector containing the Bias component and the m Matérn basis-function coefficients. By transforming the Matérn 3/2 + Bias kernel into a finite-dimensional basis-function representation, the radiation field estimation problem with a Poisson likelihood can be treated as a reduced-rank state-space model.

Let the i-th measurement location of the UAV be denoted as $\mathbf{x}_i = [x_i^{(1)}, x_i^{(2)}, x_i^{(3)}]^\top \in \mathbb{R}^3$, and let the radiation sensor measurement collected at the corresponding location be denoted as $y_i \in \mathbb{Z}_{\geq 0}$. If the entire observation dataset is denoted as $\mathbf{y} = [y_1, y_2, \ldots, y_n]^\top$, the Poisson likelihood is defined as follows.

$$p(\mathbf{y} \mid f) = \prod_{i=1}^{n} \text{Poisson}\left(y_i; \lambda_i = \exp(f(\mathbf{x}_i))\right) \tag{21}$$

Although the posterior distribution can be defined by combining the prior distribution and the likelihood, the Poisson likelihood is non-Gaussian. Therefore, the posterior distribution cannot be directly computed in closed-form Gaussian form. Accordingly, this study uses an Extended Kalman Filter (EKF) [17], which can sequentially linearize the nonlinear observation model, to update the mean and covariance of the state vector $\mathbf{w}$.

At measurement step i, the predicted state mean and covariance of the EKF are denoted as $\boldsymbol{\mu}_{i|i-1}$ and $\mathbf{P}_{i|i-1}$, respectively. When the UAV obtains the radiation sensor measurement y_i at the 3D location $\mathbf{x}_i$, the predicted count rate of the Poisson observation model is computed as follows.

$$\begin{aligned}
\hat{y}_i &= \exp\left(\boldsymbol{\phi}(\mathbf{x}_i)^\top \boldsymbol{\mu}_{i|i-1}\right) \\
\mathbf{J}_i &= \hat{y}_i \boldsymbol{\phi}(\mathbf{x}_i)^\top \\
R_i &= \hat{y}_i \\
\mathbf{K}_i &= \mathbf{P}_{i|i-1}\mathbf{J}_i^\top \left(\mathbf{J}_i \mathbf{P}_{i|i-1}\mathbf{J}_i^\top + R_i\right)^{-1} \\
\boldsymbol{\mu}_i &= \boldsymbol{\mu}_{i|i-1} + \mathbf{K}_i (y_i - \hat{y}_i) \\
\mathbf{P}_i &= (\mathbf{I} - \mathbf{K}_i \mathbf{J}_i)\mathbf{P}_{i|i-1}
\end{aligned} \tag{22}$$

Here, $\hat{y}_i$ denotes the predicted mean count rate at location $\mathbf{x}_i$, and $\mathbf{J}_i$ denotes the Jacobian obtained by linearizing the nonlinear observation function $h(\mathbf{w}) = \exp(\boldsymbol{\phi}(\mathbf{x}_i)^\top \mathbf{w})$ with respect to the state vector $\mathbf{w}$. Since the mean and variance are identical in a Poisson distribution, the observation noise variance is set to $R_i = \hat{y}_i$ in this study. In addition, $\mathbf{K}_i$ denotes the Kalman gain, and $\boldsymbol{\mu}_i$ and $\mathbf{P}_i$ denote the state

mean and covariance after incorporating the i-th radiation sensor measurement. Through this EKF-based update, the radiation field model can be sequentially updated whenever the UAV collects new sensor data, without retraining the model using the entire dataset.
Using the updated state mean $\boldsymbol{\mu}_i$ and covariance $\mathbf{P}_i$, the mean and variance of the latent log-count-rate function at an arbitrary 3D prediction location $\mathbf{x}^* = [x^{*(1)}, x^{*(2)}, x^{*(3)}]^\top$ are computed as follows.

$$\mathbb{E}[f(\mathbf{x}^*)] = \boldsymbol{\phi}(\mathbf{x}^*)^\top \boldsymbol{\mu}_i, \qquad \mathbb{V}[f(\mathbf{x}^*)] = \boldsymbol{\phi}(\mathbf{x}^*)^\top \mathbf{P}_i \boldsymbol{\phi}(\mathbf{x}^*) \tag{23}$$

However, the actual mean count rate of the radiation sensor is defined as $\lambda(\mathbf{x}) = \exp(f(\mathbf{x}))$ and thus $\lambda(\mathbf{x}^*)$ follows a log-normal distribution. Using the log-normal moment transformation, the predictive mean count rate and variance at the prediction location $\mathbf{x}^*$ are computed as follows [18].

$$\begin{aligned} \mu(\mathbf{x}^*) &= \exp\left(\mathbb{E}[f(\mathbf{x}^*)] + \frac{1}{2}\mathbb{V}[f(\mathbf{x}^*)]\right) \\ \sigma_v^2(\mathbf{x}^*) &= \left(\exp\left(\mathbb{V}[f(\mathbf{x}^*)]\right) - 1\right) \exp\left(2\mathbb{E}[f(\mathbf{x}^*)] + \mathbb{V}[f(\mathbf{x}^*)]\right) \end{aligned} \tag{24}$$

Here, $\mu(\mathbf{x}^*)$ denotes the predicted mean CPS, and $\sigma_v^2(\mathbf{x}^*)$ denotes the predictive uncertainty at the corresponding location. In this study, this predictive variance is used as an information metric in UAV informative path planning.
Consequently, the proposed ERRGP can sequentially estimate the mean and uncertainty of the 3D radiation field while incorporating count-based radiation sensor data collected by the UAV during flight in real time.

3. UAV Informative Path Planning

This section describes the informative path planning method for UAV-based 3D radiation field mapping. The proposed method uses 3D LiDAR data and radiation sensor data collected by the UAV during flight. The 3D LiDAR data are used to construct a 3D occupancy map that contains free-space and obstacle information of the surrounding environment, while the radiation sensor data are used to update the ERRGP model and compute the predictive mean and variance of the radiation field.
To select the next goal point, the ERRGP model is first updated using the accumulated measurements $(\mathbf{x}_i, y_i)$, and the predictive variance of the radiation field is then computed at each candidate location $\mathbf{x}^*$.
Subsequently, the Information Gain (IG) is defined for each candidate location $\mathbf{x}^*$ by combining the ERRGP-based predictive variance with LiDAR-based frontier information. The frontier term is used as an exploration metric that encourages the UAV to move toward regions that have not been sufficiently explored, while the ERRGP predictive variance term is used as an exploitation metric that encourages observations in regions with high uncertainty in the radiation field estimate. Finally, the UAV selects a goal point $\mathbf{x}_g^*$ with high IG from the candidate set and generates a collision-avoiding path to the selected location. Therefore, the proposed IG serves as a path planning metric that jointly considers exploration of the 3D environment and improvement of radiation field mapping accuracy.

3.1 Information Gain

First, to define the explorable region for the UAV, a 3D occupancy map is constructed using range measurements obtained from the LiDAR sensor mounted on the UAV. In the occupancy map, the boundary between free space and unknown space is defined as a frontier, which serves as an exploration indicator for expanding toward regions that have not yet been observed by the UAV [11]. In general frontier-based exploration, goal points are selected by considering the binary presence of frontiers. In contrast, this study defines a frontier weight that continuously propagates from the frontier toward the surrounding free space, as shown in Figure 1. The set of candidate cells classified as free space in the current 3D occupancy map is denoted as Fr. Here, $\mathbf{x}^* \in Fr$ represents a candidate location classified as free space in the occupancy map. In other words, $\mathbf{x}^*$ is a candidate goal point that can be selected as the next target location for the UAV. For a candidate location $\mathbf{x}^*$, if the position of the nearest frontier cell is denoted as $\mathbf{x}_f$, the frontier-based weight is defined as follows.

$$w_f(\mathbf{x}^*) = \exp\left(-\frac{d(\mathbf{x}^*, \mathbf{x}_f)^2}{2}\right), \qquad \mathbf{x}^* \in Fr \tag{25}$$

Here, $d(\mathbf{x}^*, \mathbf{x}_f)$ denotes the 3D Euclidean distance between the candidate location $\mathbf{x}^*$ and the nearest frontier cell $\mathbf{x}_f$. This continuous frontier weight assigns higher values to candidate cells near the frontier, thereby encouraging the UAV to explore regions near the boundary of unexplored areas.

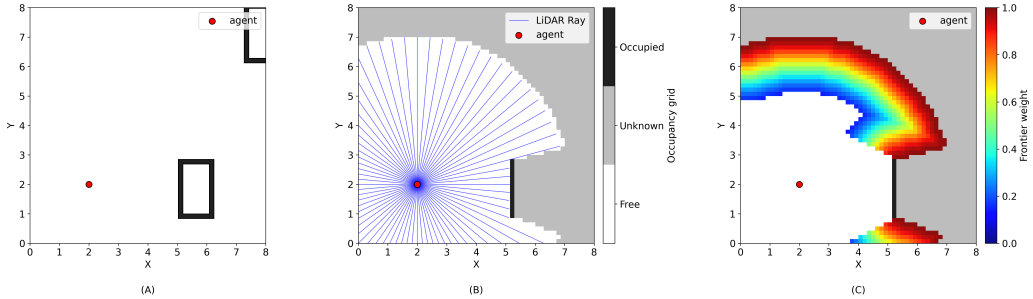


Figure 1 – Two-dimensional example of the frontier-based weight. (A) Simulation scenario, where white regions indicate free space, gray regions denote walls, and the red circle represents the robot. (B) Occupancy grid map generated from LiDAR measurements, where blue lines indicate LiDAR rays, black regions denote occupied space, gray regions denote unknown space, and white regions denote free space. (C) Spatial distribution of the frontier-based weight computed in free space around the frontier.

Next, the radiation field variance predicted by the ERRGP is used as an information acquisition metric for each candidate location $\mathbf{x}^*$. By incorporating sensor measurements that follow a Poisson distribution, the predictive variance becomes large at locations where sensor data are insufficient or where the spatial variation of the radiation field is not sufficiently explained. Therefore, the ERRGP predictive variance is used as an exploitation term for selecting locations where additional measurements are expected to be informative.

Because the predictive variance can have a wide range of values depending on the location, normalization is applied. As shown in Figure 2, conventional min–max normalization can be sensitive to a small number of large variance values and may not sufficiently represent intermediate differences in uncertainty. In contrast, log min–max normalization can reduce the influence of large values while preserving the relative uncertainty structure among candidate locations. Let the set of candidate locations be denoted as $Fr = \{\mathbf{x}_i^* \mid i = 1, \ldots, N\}$, and let the predictive variance computed from the ERRGP be denoted as $\sigma_v^2(\mathbf{x}_i^*)$. Then, the normalized variance term is defined as follows.

$$\sigma_s^2(\mathbf{x}_i^*) = \frac{\log\left(\sigma_v^2(\mathbf{x}_i^*)\right) - \min_j \log\left(\sigma_v^2(\mathbf{x}_j^*)\right)}{\max_j \log\left(\sigma_v^2(\mathbf{x}_j^*)\right) - \min_j \log\left(\sigma_v^2(\mathbf{x}_j^*)\right)}, \qquad \mathbf{x}_i^* \in Fr \tag{26}$$

Finally, the Information Gain of the candidate location $\mathbf{x}_i^*$ is defined by combining the frontier weight and the ERRGP-based normalized variance as follows.

$$IG(\mathbf{x}_i^*) = \frac{\lambda_f w_f(\mathbf{x}_i^*) + \lambda_\sigma \sigma_s^2(\mathbf{x}_i^*)}{\mathrm{counts}(\mathbf{x}_i^*)}, \qquad \mathbf{x}_i^* \in Fr \tag{27}$$

Here, λ_f and λ_σ are weighting factors that control the relative importance of the frontier-based exploration term and the ERRGP variance-based exploitation term, respectively. The term $\mathrm{counts}(\mathbf{x}_i^*)$ denotes the cumulative number of measurements already performed within a fixed radius around the candidate location $\mathbf{x}_i^*$. This term suppresses repeated selection of regions that have already been sufficiently observed and encourages the UAV to select new regions with relatively high information acquisition potential.

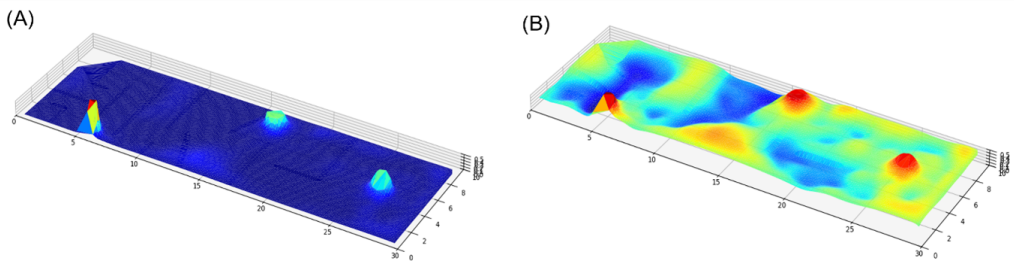


Figure 2 – Predictive variance estimated by the ERRGP. Colors transition from blue to red with increasing variance. (A) Standard min–max normalization. (B) Log min–max normalization.

3.2 Goal Selection and Path Planning

This section describes the process of selecting the next exploration goal point for the UAV using the Information Gain defined in subsection 3.1 and generating a collision-avoiding path to the selected goal point. Each candidate location $\mathbf{x}_i^*$ is associated with the information gain $v_i = IG(\mathbf{x}_i^*)$ computed using Eq. (27). Although the information gain of a goal location is used to determine where the UAV should perform the next measurement, the distance and path cost required to reach that location also affect the exploration process. Therefore, this study selects the final goal point $\mathbf{x}_g^*$ by jointly considering the information gain and the distance cost from the current UAV position.

Algorithm 1 Goal Point Selection

Require: Candidate goal points $X^* = \{\mathbf{x}_i^* \in Fr \mid i = 1,\ldots,N\}$, information gain $IG = \{v_i = IG(\mathbf{x}_i^*) \mid i = 1,\ldots,N\}$, UAV pose $\mathbf{p}$, maximum number of candidates k, candidate spacing radius r
Ensure: Goal point $\mathbf{x}_g^*$

$M \leftarrow \min(N,k)$
$\pi \leftarrow \text{argsort}(IG,\ \text{descending})$
$C \leftarrow \emptyset$
for $i \in \pi$ **do**
  if $\forall j \in C,\ \|\mathbf{x}_i^* - \mathbf{x}_j^*\| \geq r$ **then**
    $C \leftarrow C \cup \{i\}$
  end if
  if $|C| \geq M$ **then**
    break
  end if
end for
for $i \in C$ **do**
  $N_i \leftarrow \{j \in \{1,\ldots,N\} \mid \|\mathbf{x}_j^* - \mathbf{x}_i^*\| \leq r\}$
  $\bar{v}_i \leftarrow \text{average}(v_j \text{ for } j \in N_i)$
end for
for $i \in C$ **do**
  $D_i \leftarrow \|\mathbf{x}_i^* - \mathbf{p}\|$
end for
for $i \in C$ **do**
  $P_i \leftarrow 1 - \dfrac{D_i - \min_{j\in C} D_j}{\max_{j\in C} D_j - \min_{j\in C} D_j}$
end for
for $i \in C$ **do**
  $\bar{v}_{i,s} \leftarrow \dfrac{\bar{v}_i - \min_{j\in C} \bar{v}_j}{\max_{j\in C} \bar{v}_j - \min_{j\in C} \bar{v}_j}$
end for
$i^* \leftarrow \arg\max_{i\in C}(\bar{v}_{i,s} P_i)$
$\mathbf{x}_g^* \leftarrow \mathbf{x}_{i^*}^*$

Algorithm 1 shows the process of selecting the next goal point of the UAV from the candidate goal points for which IG has been computed. In Lines 1–3, the maximum number of candidates is set to $M = \min(N,k)$ to limit the computational cost. The candidate goal points are then sorted in descending order of IG, and the candidate set C is initialized. In Lines 4–11, the sorted candidates are sequentially examined, and only candidates that are separated from each other by at least the minimum distance r are added to C. This process provides spatially distributed goal point candidates among the candidates with high IG values.
In Lines 12–15, for each candidate goal point $\mathbf{x}_i^*$, the representative information gain $\bar{v}_i$ is computed by averaging the IG values of neighboring candidates within the radius r. This process is intended to select candidates whose surrounding regions have high information value, rather than relying excessively on a local peak occurring at a single cell.
In Lines 16–21, the distance D_i between the current UAV position $\mathbf{p}$ and each candidate goal point $\mathbf{x}_i^*$ is computed and converted into the distance-based accessibility score P_i. The score P_i is defined to have a larger value for candidates closer to the current UAV position and is used to account for the movement cost during goal point selection. In Lines 22–24, the neighborhood-averaged information gain $\bar{v}_i$ is transformed into $\bar{v}_{i,s}$ using min–max normalization. Finally, in Lines 25–26, the candidate that maximizes the product of the normalized information gain $\bar{v}_{i,s}$ and the distance-based accessibility score P_i is selected and defined as the final goal point $\mathbf{x}_g^*$. Therefore, the proposed goal point selection method prioritizes candidates with high information gain while reducing the likelihood of selecting candidates with excessively high access cost from the current UAV position.
Once the goal point $\mathbf{x}_g^*$ is determined, the UAV generates a collision-avoiding path to the selected goal point. In this study, the path is generated based on the Sampling-Based Information Gathering (SBIG) algorithm [19]. SBIG uses a Rapidly-exploring Random Tree (RRT)-based sampling-based planning structure and incorporates information gain into the path evaluation process. Therefore, candidate paths are evaluated by considering not only the travel distance but also the amount of information that can be acquired along the path. In the path planning process, the objective function for a candidate location $\mathbf{x}$ can be expressed as follows.

$$\max\left(IG(\mathbf{x}) - \lambda_p \mathrm{PathCost}(\mathbf{x})\right) \tag{28}$$

Here, $\mathrm{PathCost}(\mathbf{x})$ denotes the path cost required to move from the current UAV position to the candidate location $\mathbf{x}$, and λ_p is a weighting factor that controls the trade-off between information gain and movement cost. A larger λ_p assigns greater emphasis to lower-cost paths, whereas a smaller λ_p assigns greater emphasis to paths with higher information gain. In this way, the proposed method enables the UAV to move toward a 3D goal location with high information gain by simultaneously considering the ERRGP uncertainty and frontier information while avoiding obstacles based on the 3D occupancy map.

4. Numerical Simulation

To validate the performance of the proposed ERRGP-based informative path planning framework, numerical simulations were conducted in a Python-based 3D environment. The simulation was designed to evaluate whether a UAV can sequentially collect radiation measurements, update the ERRGP model in real time, construct a 3D occupancy map using 3D LiDAR measurements, and perform informative path planning to improve the radiation field estimate.

4.1 Simulation Environment Setup

The simulation environment was constructed as a 3D space with a physical size of $30\,\mathrm{m} \times 10\,\mathrm{m} \times 5\,\mathrm{m}$. The space was discretized into a 3D grid for generating the radiation field and updating the occupancy map. The UAV operates in this bounded 3D domain and collects both radiation sensor measurements and 3D LiDAR measurements during flight.
The environment contains multiple container-like shielding structures and four Cs-137 radiation sources. Each radiation source is placed inside a container structure to represent hazardous-material sources located inside shielding objects. The wall thickness of the container structures was set to $0.17\,\mathrm{m}$. The radiation sources were placed at different horizontal positions and at a fixed source height of $1.0\,\mathrm{m}$ to

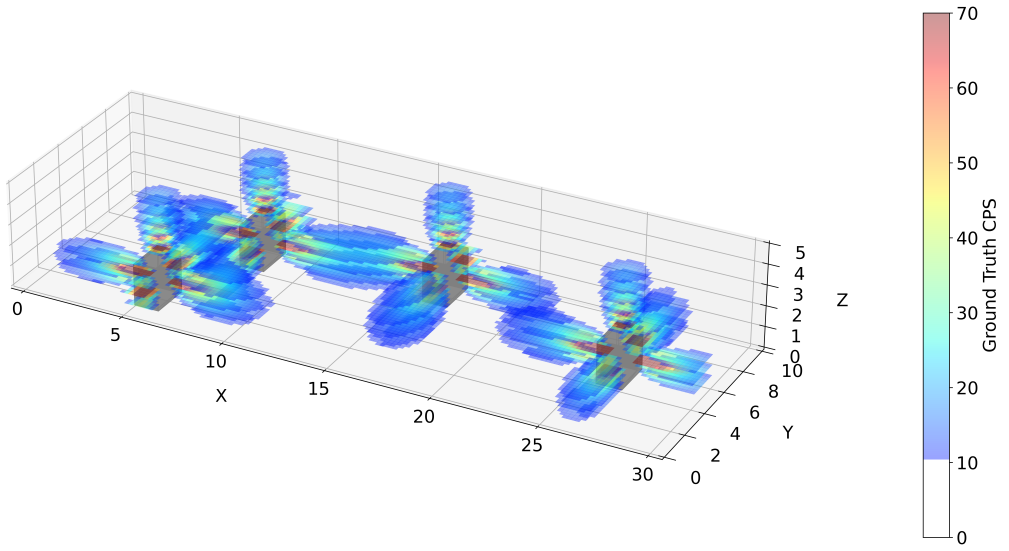


Figure 3 – Ground-truth radiation field generated in the 3D simulation environment.

generate a nonuniform 3D radiation field. This configuration allows the simulation to represent a more realistic hazardous environment in which the radiation intensity depends not only on the horizontal distance from the source but also on the UAV altitude and the shielding geometry.

Since the simulation time is negligible compared with the half-life of Cs-137, the natural radioactive decay over time is ignored. Therefore, the radiation field is assumed to be static during each simulation run, and each source emits a constant radiation intensity.

For an arbitrary query point $\mathbf{x} = [x^{(1)}, x^{(2)}, x^{(3)}]^\top \in \Omega$, the ground-truth radiation field is computed by summing the attenuated contribution from all radiation sources. Let $\mathbf{x}_s$ denote the position of the s-th radiation source and $r_s = \|\mathbf{x} - \mathbf{x}_s\|$ be the 3D Euclidean distance between the space cell and source location. The total radiation dose is modeled using an inverse-square law with air attenuation and additional attenuation caused by intersections with shielding structures:

$$\mathrm{Dose}(\mathbf{x}) = \left(\sum_{s=1}^{N_{\mathrm{src}}} \frac{A \cdot m_{\text{Cs-137}} \cdot \Gamma}{r_s^2} \cdot \exp(-\mu_{\mathrm{air}} r_s) \cdot \prod_{k=1}^{N_{\mathrm{walls}}} \exp(-\mu_{\mathrm{wall},k} L_k(\mathbf{x})) \right) + D_{\mathrm{bg}} \tag{29}$$

Here, A is the activity of the radiation source, $m_{\text{Cs-137}}$ is the mass of the Cs-137 material, Γ is the gamma-ray emission constant, and μ_{air} is the air attenuation coefficient. The term $L_k(\mathbf{x})$ denotes the intersection length between the line segment from the source to the query point and the k-th shielding structure, while $\mu_{\mathrm{wall},k}$ is the corresponding material-dependent attenuation coefficient. The constant term D_{bg} represents the background radiation level. The attenuation coefficients and radiation-related parameters were set based on the data provided by [20].

The UAV is equipped with two types of sensors: a radiation sensor and a 3D LiDAR sensor. The radiation sensor is used to collect count-based measurements, while the 3D LiDAR sensor is used to estimate the surrounding free space and obstacle regions for occupancy mapping. To generate realistic radiation sensor measurements, the simulated radiation dose $\mathrm{Dose}(\mathbf{x})$ is converted into an expected count rate using a sensor scaling factor K. Since radiation detection is a count-based process, the radiation sensor output at the UAV measurement location $\mathbf{x}_i$ is modeled as a Poisson random variable:

$$y_i \sim \mathrm{Poisson}(\lambda(\mathbf{x}_i)), \qquad \lambda(\mathbf{x}) = \frac{\mathrm{Dose}(\mathbf{x})}{K} \tag{30}$$

Here, y_i denotes the radiation count measurement collected at the UAV position $\mathbf{x}_i$, and $\lambda(\mathbf{x})$ represents the expected count rate converted from the simulated radiation dose. The scaling factor K depends on the sensor sensitivity and was set to 0.0042 in this study.

For obstacle perception, a 3D LiDAR sensor with a maximum sensing range of 5 m was assumed. The LiDAR sensor scans 360° in the horizontal direction and covers a vertical field of view from -25°

to 15°. Gaussian noise was assumed in the range measurements. The radiation sensor and the LiDAR sensor are updated synchronously at each simulation time step.

4.2 Simulation Result

The proposed UAV informative path planning framework was evaluated in a Python-based 3D simulation environment. The mapping accuracy was quantitatively evaluated using the root mean square error (RMSE) between the predicted radiation field and the ground-truth radiation field at candidate evaluation points. To evaluate statistical reliability, 100 Monte Carlo simulations were conducted under the same environment configuration, and the final performance was reported using the mean and standard deviation of the RMSE computed over all Monte Carlo runs.

In each trial, the UAV sequentially selected the next goal point based on the proposed Information Gain and collected radiation sensor data while moving along a collision-avoiding path. The collected radiation measurements were incorporated into the ERRGP model in real time, thereby sequentially updating the predictive mean and variance of the 3D radiation field. Each trial was limited to a maximum of 3,000 motion steps.

Figure 4 shows the change in RMSE as the UAV sequentially collects radiation sensor data. From the 100 Monte Carlo simulations, the mean RMSE was approximately 12.9 CPS at the initial step, decreased to approximately 11.1 CPS at 500 steps, 9.8 CPS at 1,000 steps, 8.9 CPS at 1,500 steps, 8.5 CPS at 2,000 steps, 8.3 CPS at 2,500 steps, and 8.2 CPS at 3,000 steps. These results indicate that the ERRGP model progressively learns the spatial distribution of the radiation field as sensor data accumulate, thereby improving the prediction accuracy. The reduction in RMSE was relatively large during the early stage of exploration and gradually became slower as additional sensor measurements were accumulated. This trend indicates that the UAV obtained informative measurements in the initial stage by visiting candidate regions with high information gain. As the explored region expanded, the amount of additional information obtained from new measurements decreased, resulting in a more gradual improvement in RMSE.

In addition, the UAV exploration trajectory shown in Figure 5 indicates that the proposed path planning algorithm guides the UAV to explore regions with high information gain. In particular, by using the Information Gain that combines the ERRGP predictive variance with frontier information, the UAV selected candidate locations that were informative for radiation field estimation rather than repeatedly exploring nearby regions. As a result, the proposed framework was shown to support effective exploration of information-rich regions in a 3D environment and to generate a more accurate 3D radiation field map using limited sensor measurements.

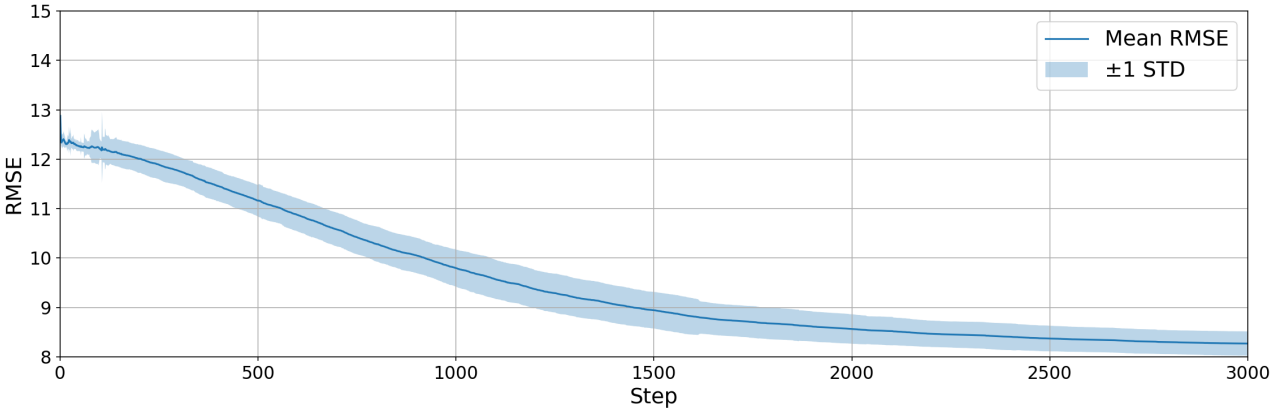


Figure 4 – Variation of RMSE with respect to the number of collected measurements.

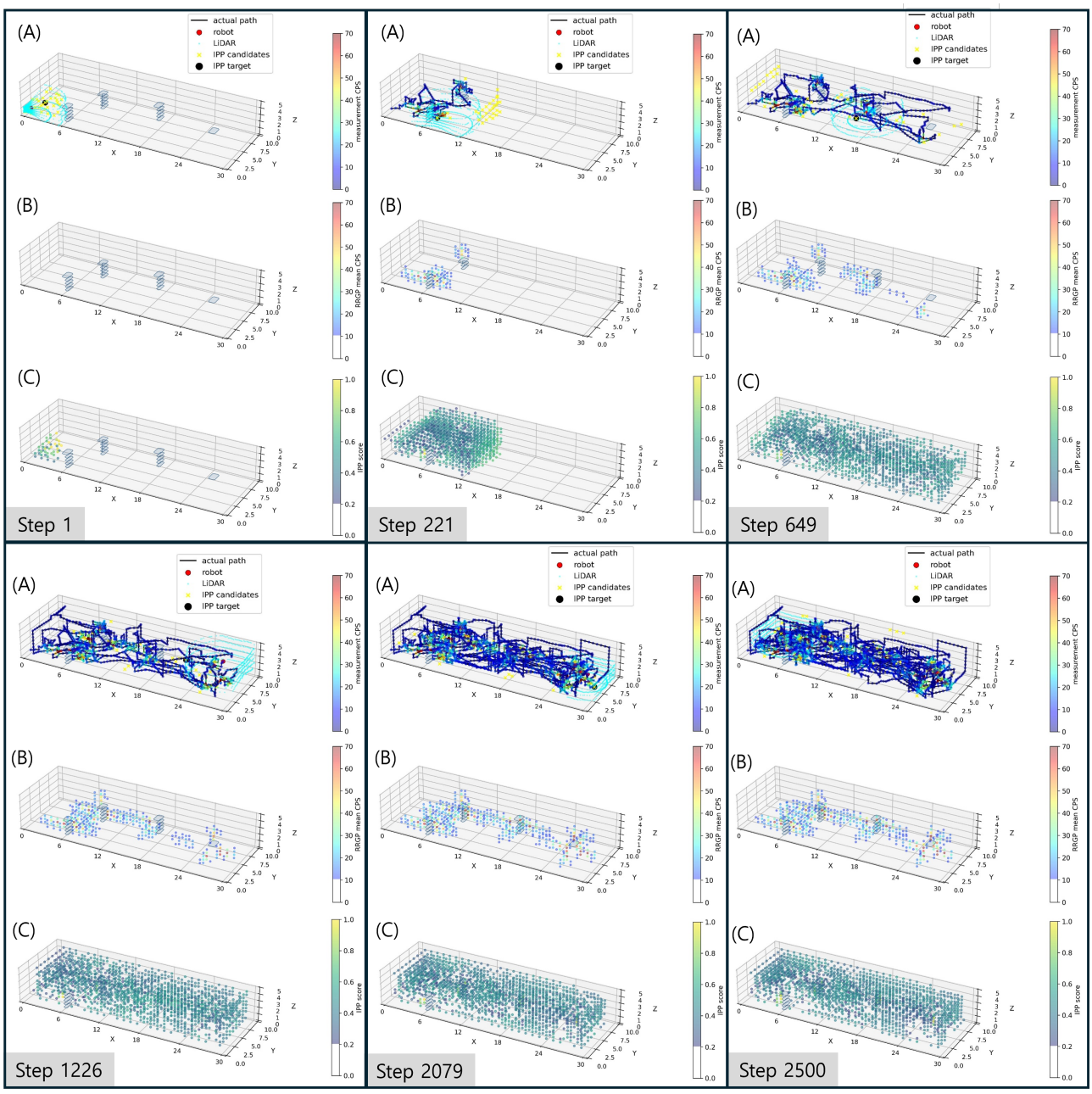


Figure 5 – Mapping progress over simulation steps: (A) radiation sensor measurements collected along the UAV trajectory, (B) ERRGP prediction result estimated from accumulated measurements, and (C) distribution of the proposed Information Gain.

5. Conclusion and Future Work

This study proposed an Extended Reduced-Rank Gaussian Process (ERRGP)-based informative path planning framework for UAV-based 3D hazardous-substance mapping. The proposed ERRGP was designed to account for count-based radiation sensor data that follow a Poisson distribution while maintaining computational efficiency through a reduced-rank structure. This enables radiation sensor data collected by the UAV during flight to be incorporated into the prediction process in real time, and allows the predictive mean and uncertainty of the 3D radiation field to be sequentially updated.

In addition, this study defined an Information Gain that combines the ERRGP predictive variance with frontier information. Based on this Information Gain, the informative path planning method selects the next goal point of the UAV by jointly considering regions with high uncertainty in the radiation field estimate and regions that have not yet been explored. This enables 3D radiation field mapping using limited sensor measurements.

The proposed framework was validated in a Python-based 3D simulation environment containing

container structures and Cs-137 radiation sources. The UAV collected measurement data using a radiation sensor and a 3D LiDAR sensor, and the mapping performance of the proposed method was quantitatively evaluated through 100 Monte Carlo simulations. The results confirmed that the proposed ERRGP-based informative path planning method can be applied to UAV-based 3D hazardous-substance mapping.

Future work will apply the proposed framework to a real UAV platform and experimentally validate its performance. To this end, actual sensor noise, measurement delay, UAV dynamic constraints, localization errors, and scattering effects caused by shielding structures will be considered. In addition, the framework will be extended to spatio-temporal mapping methods for hazardous substances that diffuse over time, such as toxic gases or chemical pollutants, by incorporating wind-field or diffusion models. Furthermore, for large-scale environments, the framework will be extended by combining multi-UAV cooperative path planning and cooperative reinforcement learning methods, enabling multiple agents to reduce redundant exploration while increasing the overall information gain.

6. Acknowledgements

This Study was supported by the 'Development Project for One-stop Platform Technology of Atomospheric Environmental Monitoring UAV System' (SN : RS-2025-02213907) funded by the ROKG

7. Contact Author Email Address

Changmin Lee: 20257167@gs.cwnu.ac.kr
Minkyu Park: mpark@cwnu.ac.kr

8. Copyright Statement

The authors confirm that they, and/or their company or organization, hold copyright on all of the original material included in this paper. The authors also confirm that they have obtained permission, from the copyright holder of any third party material included in this paper, to publish it as part of their paper. The authors confirm that they give permission, or have obtained permission from the copyright holder of this paper, for the publication and distribution of this paper as part of the ICAS proceedings or as individual off-prints from the proceedings.

References

[1] M. Dunbabin and L. Marques. Robots for environmental monitoring: Significant advancements and applications. *IEEE Robotics & Automation Magazine*, 19(1):24–39, 2012.

[2] M. A. Aniceto dos Santos and K. C. Teixeira Vivaldini. A review of the informative path planning, autonomous exploration and route planning using uav in environment monitoring. In *Proceedings of the 2022 International Conference on Computational Science and Computational Intelligence (CSCI)*, pages 445–450, 2022.

[3] H. Ardiny, A. Beigzadeh, and H. Mahani. Applications of unmanned aerial vehicles in radiological monitoring: A review. *Nuclear Engineering and Design*, 422:113110, 2024.

[4] B. Zhang, J. Cao, S. Lin, X. Li, Y. Zhang, and X. Zheng. Optimized inverse distance weighted interpolation algorithm for γ-radiation field reconstruction. *Nuclear Engineering and Technology*, 56(1):160–166, 2024.

[5] W. Yang, X. Zhang, J. Song, Y. Li, and H. Wu. Prediction of hourly pm2.5 using a space-time support vector regression. *Atmospheric Environment*, 181:12–19, 2018.

[6] K. Shukla, P. Kumar, G. S. Mann, and M. Khare. Mapping spatial distribution of particulate matter using kriging and inverse distance weighting at supersites of megacity delhi. *Sustainable Cities and Society*, 54:101997, 2020.

[7] B. A. Khuwaileh and W. A. Metwally. Gaussian process approach for dose mapping in radiation fields. *Nuclear Engineering and Technology*, 52(8):1807–1816, 2020.

[8] Andrew West, Ioannis Tsitsimpelis, Mauro Licata, Anze Jazbec, Luka Snoj, Malcolm J Joyce, and Barry Lennox. Use of gaussian process regression for radiation mapping of a nuclear reactor with a mobile robot. *Scientific reports*, 11(1):13975, 2021.

[9] A. H. Zakaria, Y. M. Mustafah, J. Abdullah, N. Khair, and T. Abdullah. Development of autonomous radiation mapping robot. *Procedia Computer Science*, 105:81–86, 2017.

[10] C Amos Kipkosgei, Yong-Kuo Liu, Justina Onyinyechukwu Adibeli, Chengjie Duan, Peng Ding, and Juqing Song. Mapping radioactive environments by use of sparse gaussian processes regression. *Annals of Nuclear Energy*, 200:110393, 2024.

[11] Haitao Liu, Jianfei Cai, Yi Wang, and Yew Soon Ong. Generalized robust bayesian committee machine for large-scale gaussian process regression. In *International Conference on Machine Learning*, pages 3131–3140. PMLR, 2018.

[12] Arno Solin and Simo Särkkä. Hilbert space methods for reduced-rank gaussian process regression. *Statistics and Computing*, 30(2):419–446, 2020.

[13] Arno Solin, Manon Kok, Niklas Wahlström, Thomas B Schön, and Simo Särkkä. Modeling and interpolation of the ambient magnetic field by gaussian processes. *IEEE Transactions on robotics*, 34(4):1112–1127, 2018.

[14] Brian Yamauchi. A frontier-based approach for autonomous exploration. In *Proceedings 1997 IEEE International Symposium on Computational Intelligence in Robotics and Automation CIRA'97.'Towards New Computational Principles for Robotics and Automation'*, pages 146–151. IEEE, 1997.

[15] C. E. Rasmussen and C. K. I. Williams. *Gaussian Processes for Machine Learning*. MIT Press, Cambridge, MA, 2006.

[16] Woosung Cho, Sung-Gyun Shin, Min-Jae Lee, Seungsoo Jang, Janghee Lee, Sangsoo Han, HangJin Jo, and Song-Hyun Kim. 3d radiation map reconstruction strategy using gaussian process regression with attenuation effects and radiation characteristics. *Nuclear Engineering and Technology*, 57(9):103612, 2025.

[17] S. Särkkä. *Bayesian Filtering and Smoothing*. Cambridge University Press, Cambridge, 2013.

[18] Jesper Møller, Anne Randi Syversveen, and Rasmus Plenge Waagepetersen. Log gaussian cox processes. *Scandinavian journal of statistics*, 25(3):451–482, 1998.

[19] Geoffrey A Hollinger and Gaurav S Sukhatme. Sampling-based motion planning for robotic information gathering. In *Robotics: Science and systems*, volume 3, pages 1–8, 2013.

[20] J. H. Hubbell and S. M. Seltzer. X-ray mass attenuation coefficients. National Institute of Standards and Technology, 2004. NIST database/resource.